First-principles study of the impact of the atomic configuration on the electronic properties of $Al_xGa_{1-x}N$ alloys

Alexandros Kyrtsos,[1,*] Masahiko Matsubara,[1] and Enrico Bellotti[1,2]
[1]*Department of Electrical and Computer Engineering, Boston University, Boston, Massachusetts 02215, USA*
[2]*Division of Materials Science and Engineering, Boston University, Boston, Massachusetts 02215, USA*

(Received 9 August 2018; revised manuscript received 22 October 2018; published 9 January 2019)

We employ first-principles calculations in the formalism of standard and hybrid density functional theory to study the electronic and structural properties of wurtzite $Al_xGa_{1-x}N$ alloys. We address the discrepancies observed in literature regarding essential electronic properties of these alloys and we investigate the dependence of these properties on the atomic ordering and composition. We show that the bowing parameter is significantly affected by the atomic ordering, ranging from zero to strong downward bowing. The effects of atomic ordering of the alloys on their band offset with respect to the pure phases are also investigated. Finally, using the effective band structure approach, we study the electronic band structure of the random alloys.

DOI: 10.1103/PhysRevB.99.035201

I. INTRODUCTION

Group III-nitride semiconductor materials have been receiving considerable attention due to their various technologically important applications. Successful applications vary from optoelectronics [1,2] and power electronics [3] to photovoltaics [4]. Specifically, $Al_xGa_{1-x}N$ alloys, hereafter called AlGaN for the sake of brevity, exhibit a wide tunability of their band gaps, ranging from 3.4 to 6.2 eV [5], corresponding to the band gaps of the pure phases of GaN and AlN, respectively. Such band gaps are ideal for deep UV industrial and medical applications. Some typical deep UV applications involve free space communications, identification of biochemical agents, counterfeit detection, disinfection, and medical diagnostics.

The thermodynamic properties of the ternary III-nitride materials have been studied by various researchers. Typically, a miscibility gap is observed for group III-nitride mixed crystals [6,7]. Specifically, a phase separation in InGaN and InAlN alloys has been observed in a wide range of compositions [8–15]. The spinodal decomposition occurring in InGaN (InAlN) is driven by the internal strain due to the excessive lattice mismatch between InN and GaN (AlN). On the other hand, the critical temperature for the appearance of the miscibility gap in the case of the AlGaN system has been shown to be much lower than the growth temperature [15,16]. Hence, excellent solubility is expected for this system. Similar to other III-V semiconductor alloy systems, long-range atomic ordering phenomena have been reported for AlGaN as well [17–22]. According to these reports, AlGaN favors the formation of self-organized superlattice structures instead of random or well-mixed alloys.

Many discrepancies are observed in the reported results of the electronic properties of the AlGaN alloys. For instance, the bowing parameter of the band gap reported by various researchers based on both experimental measurements and theoretical calculations ranges from -0.8 (upward bowing) to $+2.6$ eV (downward bowing) [23–34], even though the early findings of an upward bowing have not been reproduced [29,31]. Other technologically relevant electronic parameters, such as the AlN/GaN band offset, also exhibit large discrepancies in literature. Experimentally measured values estimate the valence band offset between 0.15 and 1.4 eV [35–38], while theoretical calculations predict a valence band offset between 0.34 and 1.6 eV [39–49]. Because of the technological importance of AlGaN, the precise knowledge of the electronic properties of this system is imperative. However, a comprehensive theoretical study of the electronic properties of this material with respect to its composition and the atomic ordering is still missing.

In this work we employ hybrid and standard density functional calculations to investigate the electronic and structural properties of the wurtzite AlGaN system, taking into account the effects of the chemical composition and the various atomic configurations of the alloys. Specifically, the stability of the ordered alloys with respect to the pure phases has been investigated via the formation energy of all the different alloy configurations that can be modeled in supercells of up to 16 atoms. Additionally, random configurations are modeled in supercells of 96 atoms. The band gaps of all the configurations are presented and the effects of the atomic ordering on the band gaps are discussed. Furthermore, the band offsets are calculated using the method of aligning the energy levels with respect to the vacuum level, employing slab calculations on both nonpolar surfaces of the wurtzite crystal. The effects of the atomic configurations on the band offsets are presented. In addition, the ionization potentials and electron affinities of the pure phases and the $Al_{0.5}Ga_{0.5}N$ system are also derived from the surface calculations. Finally, the band structures of the random alloys are obtained for the representative compositions of $x = 0.25$, 0.5, and 0.75.

The paper is organized as follows. In the following section (Sec. II), we describe the method and the details of the

*akyrtsos@bu.edu

numerical calculations. Later, in Sec. III we present the results of our calculations, and in Sec. IV we discuss the implications of our results comparing them with the available data in literature. Section V concludes the paper.

II. METHOD

We employ density functional theory (DFT) [50,51] calculations using the projector augmented wave (PAW) [52,53] method as implemented in the Vienna *ab initio* simulation package (VASP) [54]. The exchange-correlation energy is treated differently depending on the task at hand. The different approaches used are the generalized gradient approximation (GGA) in the PBE [55,56] and PBEsol [57] variances, as well as hybrid functional calculations in the parametrization by Heyd, Scuseria, and Ernzerhof (HSE) [58,59]. In the case of the hybrid functional calculations we employ a composition-dependent mixing parameter for the Hartree-Fock exchange, ranging linearly from $a = 0.28$ for pure GaN ($x = 0$) to $a = 0.32$ for pure AlN ($x = 1$). The cutoff energy of the plane-wave basis set was fixed at 500 eV. All the calculations were spin polarized and the gallium $3d$ electrons were treated as valence electrons.

The atomic configurations for the study of the alloys at different compositions were generated using the ATAT code [60,61]. Supercells of up to 16 atoms were employed, yielding 401 distinct atomic configurations including the pure phases. The sampling of the Brillouin zone was performed using Γ-centered k-point meshes. In order for the results to be consistent, the same k-point density of at least 1000 k points per reciprocal atom was used throughout the calculations. Additionally, random configurations were investigated using supercells of 96 atoms with a $2\times 2\times 2$ k mesh. The random configurations were constructed by randomly occupying the lattice sites, given the constraint that the cations may occupy cation sites only. The atomic configurations were optimized using a force criterion of 10^{-3} and 10^{-2} eV/Å for the GGA and HSE calculations, respectively, allowing for volume relaxations as well.

The relative stability of the alloys was investigated using the formation energy defined in Eq. (1) as the difference of the total energy of the alloy and the weighted sum of the constituent pure phases:

$$\Delta H = E_{\text{tot}}^{\text{AlGaN}} - (1-x)E_{\text{tot}}^{\text{GaN}} - xE_{\text{tot}}^{\text{AlN}}. \tag{1}$$

Typically, a concave dependence of the formation energy on the composition x of the alloy implies that the pure phases are more stable than the intermediate alloys. Similarly, a convex dependence indicates the existence of alloy ground states. Although the general dependence might be concave, regions of local stability might appear. The local stability of a configuration σ can be determined by the local potential depth $\Delta(\sigma)$ [62,63], defined as

$$\Delta(\sigma) = \Delta H^{\sigma} - \frac{x(\sigma)-x(\alpha)}{x(\beta)-x(\alpha)}\Delta H^{\beta} - \frac{x(\beta)-x(\sigma)}{x(\beta)-x(\alpha)}\Delta H^{\alpha}, \tag{2}$$

where α and β are the two configurations on either side of σ such that $x(\alpha) < x(\sigma) < x(\beta)$. In regions of local convexity, $\Delta(\sigma)$ is negative and the states are said to be locally stable.

A number of different methods have been developed for aligning the energy levels of the interfacing semiconductor materials. Common methods are the alignment of the levels with respect to the vacuum level following Shockley-Anderson's electron affinity rule [64–66], characteristic core marker levels in the band structure [67,68], charge neutrality levels [69], branch point energies [70,71], and via the heterostructure alignment approach [72,73]. In this work, the chosen method was the alignment with respect to the vacuum level, which is used as a common reference level for the two interfacing materials. Following this approach, the band offsets obtained refer to unstrained conditions and they are usually called natural band offsets. In real interfaces, the lattice mismatch causes strain at the interface, affecting the alignment of the energy levels. The incorporation of strain effects can be performed *a posteriori* using volume deformation potentials [71,74].

The alignment with respect to the vacuum level requires surface calculations. There are two main considerations for such calculations. First, the slab that models the surface should be thick enough, so that a bulk-like region is reproduced at the center of the slab. Second, the vacuum region surrounding the slab should be large enough to eliminate any interactions with the periodic images of the slab. Specifically, in the case of systems such as AlGaN where polarization fields are present in the crystal, further considerations should be taken into account. For such cases, surfaces along nonpolar directions should be used in order to avoid polarization fields along the perpendicular direction to the surface, which would otherwise affect the alignment of the energy levels. In the case of wurtzite GaN and AlN, the $[10\bar{1}0]$ and $[11\bar{2}0]$ directions result in nonpolar planes. These planes are commonly called m and a planes, respectively.

All the calculations regarding the band alignments were performed using the HSE formalism. For the a-plane surfaces, a slab of 14 atomic layers and a vacuum region of 24 Å was employed. In the case of the m-plane surfaces, the thickness of the slab was 20 atomic layers with a vacuum region of 24 Å. The atoms were allowed to relax with a force convergence criterion of 0.02 eV/Å. In order to obtain the potential values corresponding to the vacuum and the bulk regions of the surface, the planar and the macroscopic average of the electrostatic potential are required. The planar average of the electrostatic potential $\bar{V}$ is obtained as the average of the electrostatic potential on planes parallel to the surface. The macroscopic average of the electrostatic potential $\tilde{V}$ is derived by the planar average [75]. The procedure to obtain $\tilde{V}$ from $\bar{V}$ is by taking the moving averages of $\bar{V}$ over distances of one unit cell along the direction perpendicular to the surface. Finally, the alignment of the energy levels with respect to the vacuum level is achieved by aligning the average bulk potential obtained by the bulk calculations with the value of $\tilde{V}$ at the center of the slab.

Typically, the concept of the electronic band structure of solids is meaningful only for periodic crystals where Bloch's theorem is valid. However, the alloys are inherently random, missing long-range periodicity. Traditionally, the methods to treat the electronic structure of alloys include the coherent potential approximation (CPA) [76] and the virtual crystal approximation (VCA) [77]. These methods enforce an

artificially high symmetry and are unable to capture the effects of randomness and local relaxations in alloys. In this work, the electronic structure of random alloys was investigated employing the effective band structure (EBS) method [78,79]. Using this approach, the $\vec{k}$ dependence of the energy is extracted from standard supercell calculations.

The supercell used for the modeling of the alloy is essentially derived by a certain replication of the primitive cell along the spatial directions. Therefore, both the direct and the reciprocal basis vectors of the supercell and the primitive cell are connected by a simple matrix multiplication. This notion allows for the band structure of the supercell to be unfolded into the Brillouin zone of the primitive cell. The spectral weight [79] corresponds to the amount of the Bloch character of a set of states of the primitive cell that is preserved in a state of the supercell. If the supercell is a simple replication of the primitive cell, as in the case of bulk calculations, the spectral weights would take only integer values. However, for alloy calculations, the spectral weights would take any real value.

The random alloys of compositions $x = 0.25$, 0.5, and 0.75 were modeled using a supercell of 96 atoms. The EBS calculations were performed using the BandUP code [80,81] in the PBE formalism. Both the atomic positions and the volume of the structures were relaxed in order to eliminate any stress-related effects.

III. RESULTS

A. Structural properties

The crystallographic parameters of the wurtzite phase of GaN and AlN were obtained using the PBE, PBEsol, and HSE functionals. The results are in excellent agreement with previous experimental [5,82] and theoretical [83,84] data. In the case of the PBE functional, the lattice constants of GaN and AlN are overestimated by 1% and 0.5%, respectively. Furthermore, the band gaps are severely underestimated due to the known band-gap error of standard DFT. The PBEsol functional is optimized to reproduce the experimental structural parameters, thus, it yields excellent agreement with the experimental data. However, it also fails to reproduce the experimental band gaps, similarly to the case of PBE. In the case of the HSE functional, both the structural parameters and the band gaps are in excellent agreement with the experimental data. The results for all the functionals are summarized in Table I. In an effort to reduce the computational cost, the PBEsol relaxed structures were used as a starting point for the HSE calculations.

According to Vegard's law [85], the lattice constant of a solid solution of two constituents follows a linear relationship given by the rule of mixtures, such that $a_x^{AB} = (1-x)a_A + xa_B$. In the case of AlGaN, the role of the lattice constant of the wurtzite crystal is substituted by the pseudocubic lattice constant, defined as the cube root of the normalized volume of the supercell. Figure 1 shows the pseudocubic lattice constant with respect to the composition of the alloy obtained by PBE, PBEsol, and HSE calculations. The volumes of the supercells and the atomic positions were fully relaxed. The values of the pseudocubic lattice constant among different configurations of the same composition were found identical. The pseudocubic lattice constant of the intermediate compositions obtained by the three different functional calculations is in excellent agreement with the straight line connecting the pure phases. Therefore, no bowing is observed for the lattice constant. Instead, the results are coherent with Vegard's law.

TABLE I. Crystallographic parameters and band gaps of the wurtzite GaN and AlN obtained by PBE, PBEsol, and HSE calculations. The experimental band gaps and structural parameters are obtained by Refs. [5] and [82], respectively.

	Method	a (Å)	c (Å)	u	E_g (eV)
GaN	PBE	3.217	5.242	0.377	1.72
	PBEsol	3.180	5.181	0.377	1.91
	HSE	3.178	5.168	0.377	3.45
	Expt.	3.190	5.189	0.377	3.39
AlN	PBE	3.126	5.010	0.382	4.07
	PBEsol	3.111	4.979	0.382	4.13
	HSE	3.095	4.950	0.382	6.14
	Expt.	3.110	4.980	0.382	6.2

Supercells of 4, 8, 12, and 16 atoms were employed for the investigation of the stability of the alloys with respect to the pure phases. In total, 401 unique atomic configurations were considered including the pure phases. The alloys were studied for 11 different compositions. The PBE functional was employed for all the calculations and the results shown in Fig. 2 were obtained using Eq. (1). The lowest formation energy of each composition is indicated with a red diamond in the figure. The general concavity of the results indicates the lack of ground states for the intermediate compositions. However, regions with local convexity are observed for $x = 0.333$, 0.5, and 0.667. Hence, these compositions result in locally stable ground states. An estimation of the local potential depths can be obtained using Eq. (2). For the case of $x = 0.333$, 0.5, and 0.667 the local potential depths are -1.65, -1.24, and -1.82 meV/cation, respectively.

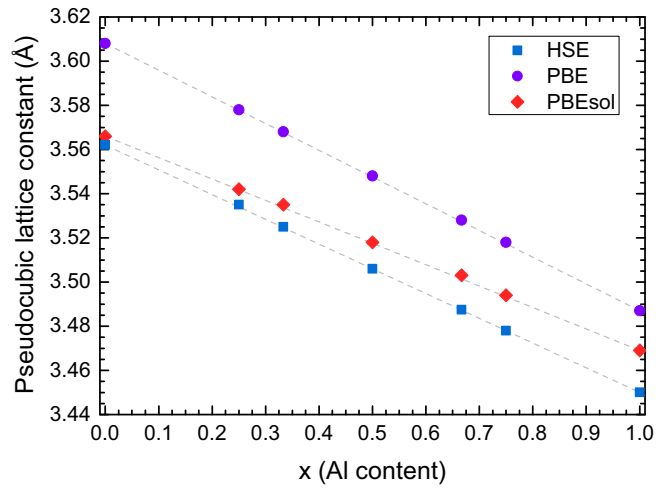

FIG. 1. The pseudocubic lattice constant, i.e., $V_{cell}^{1/3}$, obtained using the HSE, PBE, and PBEsol functionals for different alloy compositions.

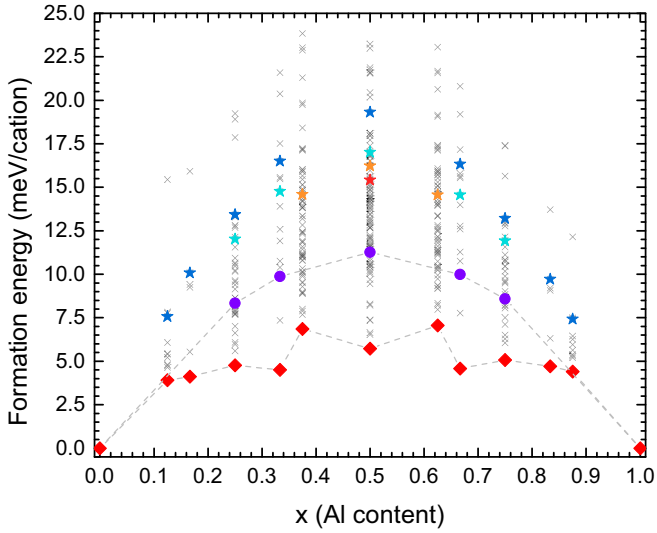

FIG. 2. Formation energies of the AlGaN alloys using supercells of 4, 8, 12, and 16 atoms, obtained by PBE calculations. The diamonds indicate the lowest formation energy of each composition while the circles correspond to the formation energies of the random alloys. The stars indicate the formation energies of the superlattice configurations along the [0001] direction. The lines are drawn to guide the eye.

The formation energies of random alloys with aluminum content of $x = 0.25$, 0.333, 0.5, 0.667, and 0.75 were calculated using supercells of 96 atoms. For these calculations, 25 distinct randomly generated structures were employed for each composition. The mean value and the standard error of the calculated formation energies were 8.34 ± 0.07, 9.9 ± 0.1, 11.3 ± 0.1, 9.98 ± 0.09, and 8.58 ± 0.07 meV/cation for $x = 0.25$, 0.333, 0.5, 0.667, and 0.75, respectively. Figure 2 shows the values of the formation energies of the random alloys as violet circles. In this case, the formation energies follow a concave trend and the local convexity is lost. Even though the random structures are not the most energetically favorable, they still yield lower formation energies compared to other ordered configurations. For instance, the superlattices along the [0001] were not found to be thermodynamically favorable. Their formation energies, shown as stars in Fig. 2, were significantly higher, compared to the random configurations. These configurations will be discussed in more detail as a special case later.

Regarding the dependence of the atomic ordering on the formation energies of the alloys, all the compositions follow similar trends. Typically, poor mixing of the cations yields higher formation energies. In this context, poorly mixed configurations refer to configurations exhibiting long-range ordering such as multilayer superlattice structures. On the other hand, well-mixed structures refer to configurations where the cations are uniformly distributed, exhibiting short-range ordering or no ordering at all. The lowest formation energy of a given composition is obtained for well-mixed structures. Specifically, the atomic configuration yielding the lowest formation energy for composition x is the same also for the composition $1 - x$, by interchanging the aluminum and gallium atoms. In general, the results indicate that the dependence of

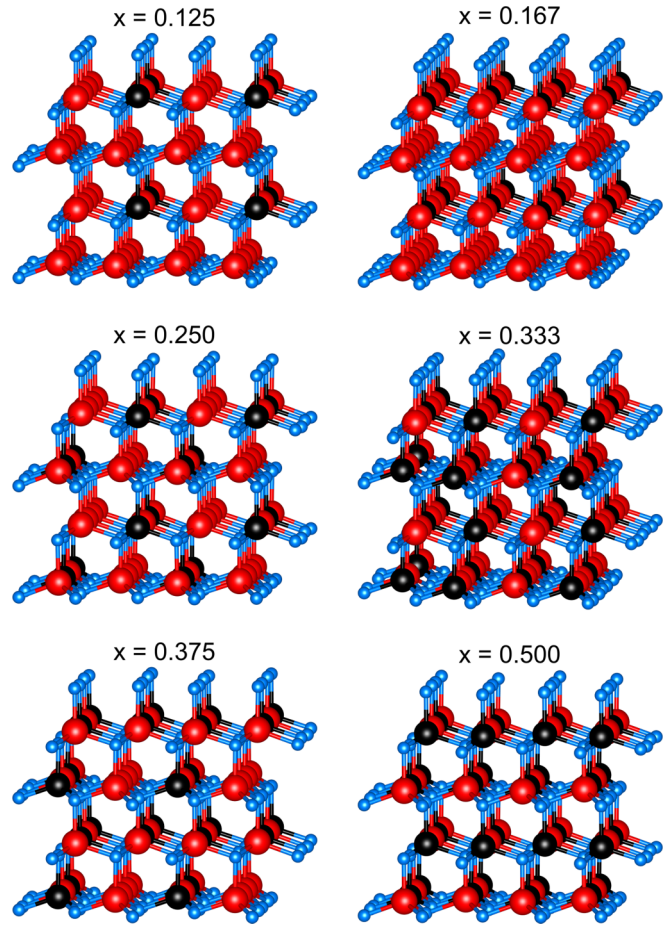

FIG. 3. The atomic configurations yielding the lowest formation energies for compositions of $x = 0.125$, 0.167, 0.25, 0.333, 0.375, and 0.5. The large red and black atoms correspond to gallium and aluminum, respectively, while the small blue atoms refer to nitrogen.

the formation energy on the ordering of the alloys is similar for $x < 0.5$ and $x > 0.5$, considering the interchange of the cations. Figure 3 shows the atomic configurations yielding the lowest formation energies for compositions up to 50%. For $x > 0.5$, the configurations are identical with the cations being interchanged. In the case of the first two compositions that were investigated, namely $x = 0.125$ and 0.167, the formation of monolayers of pure gallium along the [0001] direction is observed. Similarly, the formation of aluminum monolayers along the same direction is observed for $x = 0.875$ and 0.833. For increasing aluminum content, this behavior disappears until $x = 0.5$ is reached where perfect mixing is observed. For $x = 0.25$ and 0.375, layers of pure gallium appear in both nonpolar directions of the crystal. Finally, in the case of $x = 0.333$, monolayers of pure aluminum and bilayers of pure gallium are formed along the $[11\bar{2}0]$ direction. This structure is also observed in InGaN of the same composition [86,87].

As mentioned before, we consider the ordering of the superlattices along the [0001] direction as a special case. These configurations can be distinguished in terms of the number of consecutive pure layers of the minority cation, i.e., Al and Ga for $x < 0.5$ and $x > 0.5$, respectively. However, for supercells of up to 16 atoms, like the ones used in our calculations, there

are limitations on the number of consecutive layers of the minority cation that can be modeled for the different compositions. In the case of $x = 0.125$ and 0.167 where aluminum is the minority cation, structures of one and two consecutive aluminum layers can be modeled. Three consecutive layers can be modeled for $x = 0.375$, while up to four consecutive layers can be investigated for $x = 0.5$. Consequently, the same is true for the complementary compositions with $x > 0.5$, where gallium is the minority cation. The formation energies of these configurations are shown as stars in Fig. 2. Blue, cyan, orange, and red stars correspond to one, two, three, and four consecutive layers of the minority cation, respectively. The formation energy decreases with increasing consecutive layers of the minority cation.

B. Electronic properties

1. Band gaps

The standard DFT approach usually fails to predict important electronic properties of materials such as the band gap. In this matter, hybrid functionals have greatly improved the agreement of calculations with experimental data. However, their benefit comes with increased computational cost. Hence, large-scale hybrid functional calculations are still prohibitive. Even though standard DFT lacks the accuracy of hybrid functionals, it produces qualitatively similar results. For the investigation of the band gaps, PBE calculations were employed primarily, while HSE calculations were used in some characteristic cases for comparison and verification.

The band gaps obtained by both the PBE and the HSE calculations exhibit large variations as shown in Fig. 4. The variation of the band gaps generally increases with increasing aluminum content. The dependence of the band gap on the structural properties of the alloys exhibits similarities for all compositions. Typically, the well-mixed configurations with low formation energy yield large band gaps for all the investigated compositions. On the contrary, poorly mixed configurations with long-range ordering result in smaller band gaps.

Among all the band gaps shown in Fig. 4, it is worth noting some characteristic cases. First, a straight line connecting the band gaps of the pure phases is used as a reference. The largest band gap of each composition follows closely this straight line. Specifically, these configurations correspond to the lowest formation energy configurations shown in Fig. 2. Furthermore, the band gaps of the random alloys, shown as crosses in Fig. 4, are obtained using 25 randomly generated 96-atom supercells. In the case of the PBE calculations, the band gaps of the random alloys presented in Fig. 4 correspond to the mean values of the different random configurations. The mean values and the standard errors of the band gaps of the random alloys obtained by the PBE calculations are 2.268 ± 0.002, 2.445 ± 0.002, 2.810 ± 0.003, 3.189 ± 0.002, and 3.386 ± 0.001 eV, for $x = 0.25, 0.333, 0.5, 0.667$, and 0.75, respectively. The last characteristic case is the case of superlattices along the [0001] direction. This case is of particular importance since these structures were found to exhibit the smallest band gaps.

The critical feature determining the band gap of the [0001] direction superlattices was the number of consecutive atomic layers of the minority cation. Specifically, more consecutive layers of the minority cation yield lower band gaps. In Fig. 4, the band gaps of configurations of one, two, three, and four consecutive layers of the minority cation along the [0001] direction are shown in blue, cyan, orange, and red. Increasing the thickness of consecutive layers of the minority cation causes a decrease in the band gap. These findings support the all-electron DFT results of Cui *et al.* [88], where the band gaps of GaN/AlN superlattices have been investigated. As a final note, somewhat mixed layers along the same direction also resulted in small band gaps.

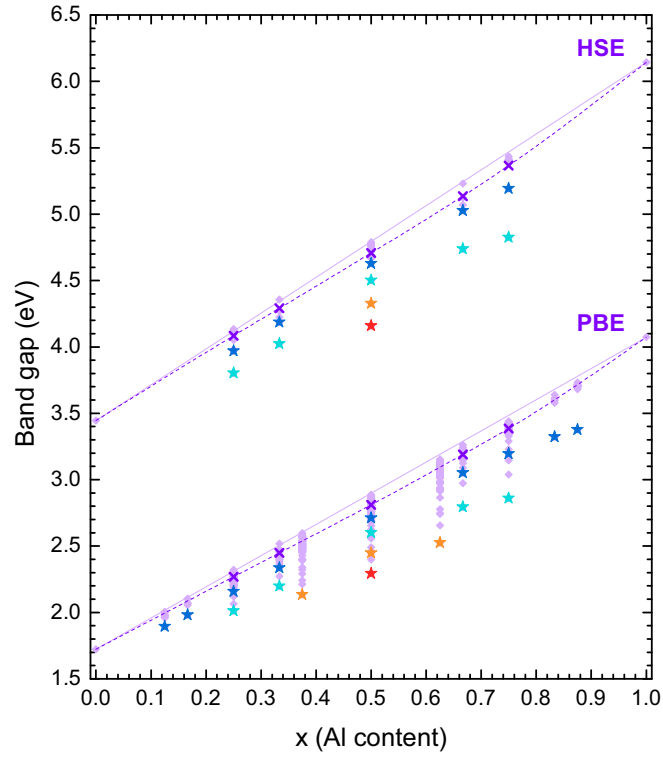

FIG. 4. The band gaps of the AlGaN alloys obtained by PBE and HSE calculations, using supercells of 4, 8, 12, and 16 atoms. The stars indicate the band gaps of superlattice configurations along the [0001] direction. The crosses correspond to the band gaps of the random alloys. The lines connecting the band gaps of the pure phases and the random alloys are drawn to guide the eye.

In order to reduce the computational cost, HSE calculations were performed only for compositions of $x = 0.25$, 0.333, 0.5, 0.667, and 0.75. Some indicative cases were investigated at these compositions. These cases include the lowest formation energy configurations, the random alloys, the superlattices along the [0001] direction, and a few other randomly selected configurations. The band gaps of the random alloys were computed using a single configuration for each composition. This configuration was chosen based on the PBE calculations to yield a band gap close to the mean band gap. Quantitatively, the band gaps are larger since HSE mitigates the underestimation of the band-gap problem which is prevalent in standard DFT calculations. Qualitatively, though, the results shown in Fig. 4 are identical for both functionals. Hence, useful information can be obtained from

PBE calculations at a fraction of the computational cost of HSE calculations.

An important parameter that can readily be extracted from the calculations is the bowing of the band gaps for different compositions. The bowing parameter b is a measure of the deviation of the band gaps from linearity, defined in terms of equation

$$E_g = (1-x)E_g^A + xE_g^B - bx(1-x), \tag{3}$$

where E_g^A and E_g^B are the band gaps of the pure phases A and B, respectively. In the case of $b > 0$ (downward bowing), the dependence of the band gap of the alloy on the composition is concave, while for $b < 0$ (upward bowing) the dependence is convex. The largest band gap of each composition follows closely the straight line connecting the band gaps of the pure phases in Fig. 4, thus indicating zero bowing. However, the random alloys yield a bowing parameter of 0.36 eV both for PBE and HSE calculations. Considering only $x = 0.25$ and 0.333, a good fit is achieved for $b = 0.25$ eV, while considering only $x = 0.667$ and 0.75, a value of $b = 0.5$ eV is obtained. Therefore, the results show stronger bowing for increasing Al content. Based on the results presented in Fig. 4, larger positive bowing parameters can be derived by considering other configurations that deviate even more from linearity.

2. *Band alignments*

The band alignments were obtained using HSE calculations following the method of aligning the energy levels with respect to the vacuum level. Figure 5 shows the electrostatic potential obtained by the GaN m-plane slab. The macroscopic average of the potential is calculated as described in Sec. II. The atomic positions of the relaxed slab are also included in the figure for reference. The adequateness of the size of the supercell can be verified by the flatness of the planar average of the electrostatic potential in the vacuum region, as shown in Fig. 5. The structural parameters in the center of the slab were identical to the ones of the bulk. In addition to the structural parameters, the flatness of the macroscopic average of the electrostatic potential, shown with a dashed line in Fig. 5, is also indicative that the thickness of the slab was adequate. Regarding the surfaces of the slab, reconstructions similar to the ones reported by Csik *et al.* [89] for the CdSe wurtzite system were observed. There is an outward and inward relaxation for the anions and the cations, respectively, for both the m- and the a-plane surfaces.

In addition to the adequate size of the supercell and the polarity of the surfaces, one more condition should be considered for the slab calculations of the AlGaN alloys. Moses *et al.* [39] have shown that the stoichiometry of the alloy should be preserved in each layer parallel to the surface. Otherwise, even if the total composition over the whole slab is maintained, the potential alignment becomes sensitive to the positioning of the layers of different stoichiometry within the slab. However, the fulfillment of this condition gives rise to challenging practical issues. First, alloy compositions of either small or large Al content require very large supercells in order to achieve a constant stoichiometry for every layer, making these calculations computationally prohibitive. Second, even if such calculations were computationally feasible, it would be possible to model only a small fraction of the available configurations.

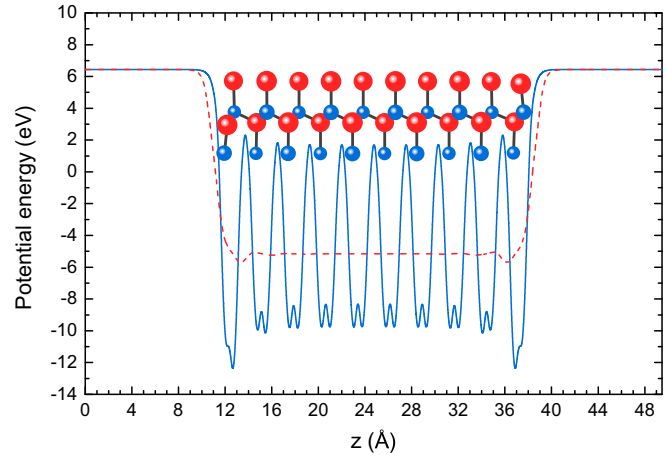

FIG. 5. The planar average (solid curve) and macroscopic average (dashed curve) of the electrostatic potential for a fully relaxed GaN m-plane slab, obtained by HSE calculations. The large red and the small blue spheres correspond to Ga and N atoms, respectively.

For our band offset calculations, in addition to the pure phases, the $Al_{0.5}Ga_{0.5}N$ alloy was also considered as an intermediate point. This particular alloy exhibits the highest number of possible atomic configurations. Thus, the effects of different atomic configurations on the band offsets can be investigated. In order to study these effects, a well and a poorly mixed configuration should be used. As mentioned earlier, the low formation energy configurations yielding large band gaps are typically well-mixed configurations, while high formation energy configurations yielding small band gaps are typically highly ordered structures. Therefore, the first case refers to a configuration of low formation energy and large band gap while the second case refers to a configuration of high formation energy and small band gap.

An obvious choice for the case of the well-mixed configuration is the one shown in Fig. 3 for $x = 0.5$. This configuration yields the lowest formation energy and the largest band gap among all the investigated $Al_{0.5}Ga_{0.5}N$ alloys. Employing this structure, the stoichiometry of the alloy is maintained for both nonpolar surfaces, over all the layers of the slab. The first two structural models in Fig. 6 illustrate the m- and a-plane surfaces corresponding to this configuration.

For the second case, the one of a poorly mixed configuration, a number of different options are available that could serve the purpose. The effects of slightly different ordering can also be investigated by considering two different configurations instead of one. In order for the results to be comparable, though, the band gaps of the two configurations should be similar. In this work, two poorly mixed configurations of similar band gap were employed. Each configuration was used for one of the nonpolar surfaces. Hence, one was employed for the surface along the $[11\bar{2}0]$ direction while the other was used for the $[10\bar{1}0]$ direction. For the m-plane surface, the chosen configuration forms a bilayer superlattice along the $[10\bar{1}0]$ direction of the crystal. The third model shown in Fig. 6, cor-

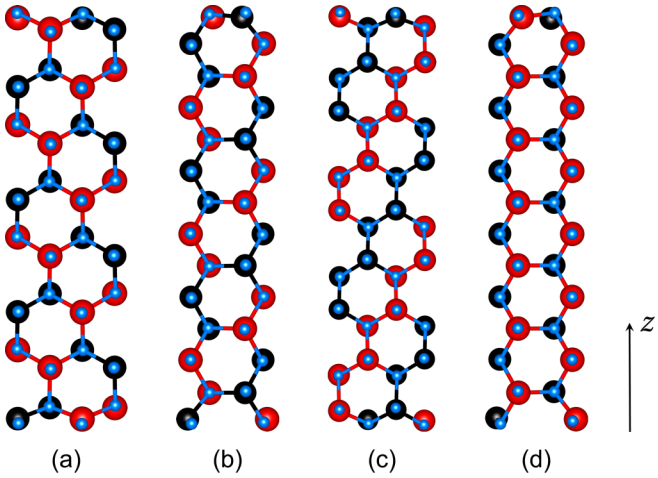

FIG. 6. The relaxed surfaces of the large band-gap $Al_{0.5}Ga_{0.5}N$ configuration for the m plane (a) and a plane (b). The small band-gap configurations for the m- and a-plane calculations are shown in (c) and (d), respectively.

responding to this configuration, illustrates the formation of this superlattice. Since the surface parallel to the superlattice is not suitable for the calculations because the stoichiometry is not preserved in every layer, another equivalent m plane, rotated by 60° with respect to the direction of the superlattice, is used. For the a-plane surface, the superlattice of alternating cation monolayers along the [0001] direction was used. The corresponding slab is shown as the last model in Fig. 6. In both configurations, the stoichiometry in planes parallel to the surface is preserved.

The results for the valence band and the conduction band offsets are presented in Fig. 7. The m- and a-plane slab calculations indicate a valence band offset of 0.46 and 0.40 eV,

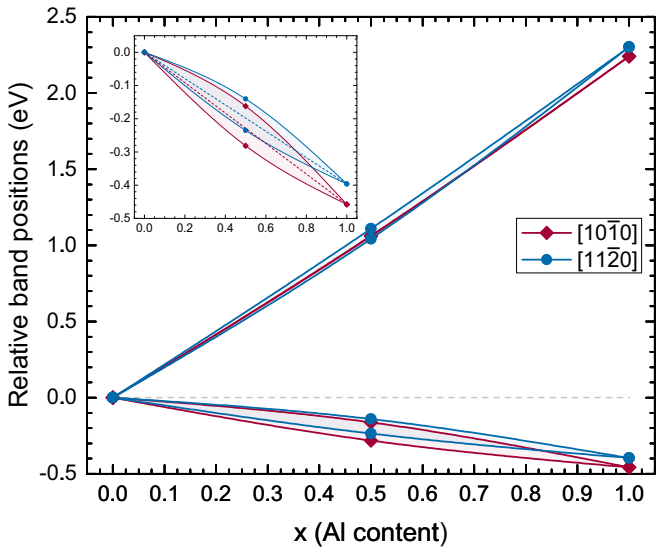

FIG. 7. The valence band and conduction band offsets of $Al_{0.5}Ga_{0.5}N$ and pure AlN with respect to GaN, calculated for both nonpolar directions of the wurtzite crystal. The inset shows just the valence band offset and the solid lines are drawn to guide the eye, while the dashed lines connect the pure phases linearly.

respectively, between pure GaN and AlN. These results fall within the range of the experimental values of 0.15 to 1.4 eV [35–38], and are in good agreement with previous calculated data [39]. In the case of $Al_{0.5}Ga_{0.5}N$, the valence band edge shift with respect to pure GaN ranges between 0.16 and 0.28 eV based on the calculations of the m-plane surface. The a-plane surface calculations yield a range between 0.14 and 0.24 eV. The inset in Fig. 7 shows a magnified version of the valence band alignment results, indicating the effect of the different atomic configurations. The inset in Fig. 7 also demonstrates a hypothetical linear dependence of the band offset on the composition. In the case of poorly mixed alloys, an upward deviation from linearity is observed while the opposite is true for well-mixed alloys. This effect is not observed in the case of the conduction band offsets.

Other properties such as the ionization potentials (IP) and the electron affinities (EA) can also be derived from the slab calculations. The IP is defined as the valence band maximum referenced to the vacuum level, while the EA corresponds to the conduction band minimum referenced to the vacuum level. The IP/EA of GaN and AlN is calculated to be 6.49/3.05 and 6.95/0.81 eV, respectively, using the m-plane surface calculations. The a-plane surface calculations yield the values of 6.55/3.11 and 6.95/0.80 eV for GaN and AlN, respectively. These results are in good agreement with previous theoretically determined values of 3.18 and 1.01 eV for the EA of GaN and AlN, respectively [39]. Our calculated EA of GaN is in excellent agreement with the experimental value of 3.1 ± 0.2 eV reported by Grabowski *et al.* [90]. Other experimental values for GaN range from 2.6 to 3.5 eV [91–93]. In the case of AlN, the experimental values of the EA range from 0 to 1.9 eV [92,94]. It should be noted that the accurate experimental determination of the EA is challenging due to surface contamination and oxidation of the samples.

Regarding the case of $Al_{0.5}Ga_{0.5}N$, the IP/EA of the large band-gap configuration was obtained both by the m- and a-plane surface calculations. The calculated values were 6.77/1.98 and 6.79/2.00 eV, respectively. Hence, both surfaces yield almost identical results. In the case of the small band-gap configurations, the IP/EA of the first structure, obtained by the m-plane surface was 6.65/1.99 eV. The IP/EA calculations of the other small band-gap configuration, using the a-plane surface, yielded the values of 6.69/2.06 eV. As observed by these results, the EA of the small and large band-gap configurations are quite similar. The difference in the band gaps of these configurations arises mainly from the IP. Therefore, the main reason of the band-gap difference is the lower positioning of the valence band maximum with respect to the vacuum level.

3. Effective band structures

The effective band structure introduces the concept of the electronic band structure for solids where the long-range periodicity is missing, as in the case of random alloys. Typically, the $\vec{k}$ dependence of the energy is represented by lines of zero broadening in a band structure diagram. A useful quantity in EBS calculations is the spectral function of the energy, which is the energy dependence of the spectral weight, as defined in Sec. II, for a given k point. For a pristine crystal, the spectral function of a given k point would be a set of δ functions of

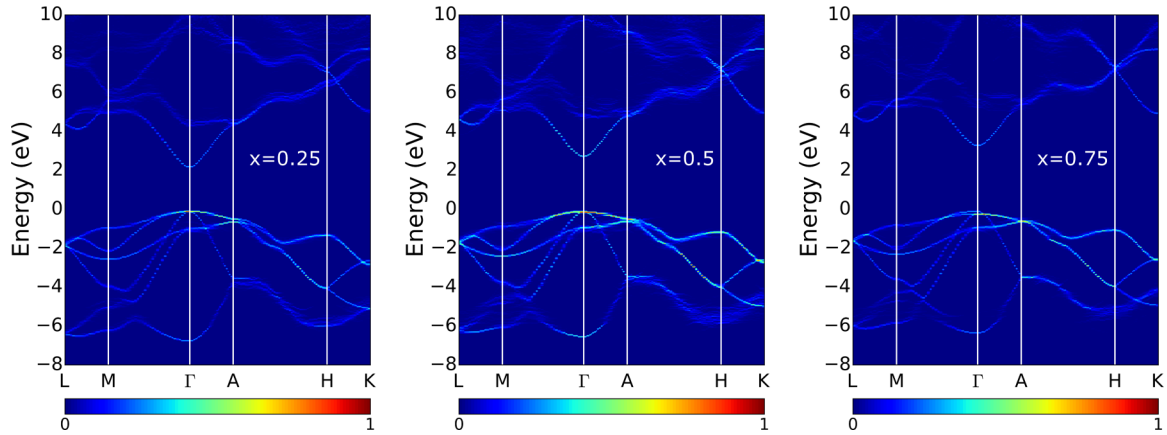

FIG. 8. The effective band structures of the random alloys for Al content of 25% (left), 50% (middle), and 75% (right) obtained by PBE calculations. The spectral weights are normalized in the range between 0 and 1 for all the compositions.

integer amplitude. In the case of alloys, the δ functions are broadened, introducing perturbations to the band structure.

The EBS of the random alloys was obtained for the representative cases of $x = 0.25$, 0.5, and 0.75. Typically, two different approaches are available for obtaining the EBS of an alloy. The first approach relies on the sampling of a large number of alloy supercells followed by the statistical averaging of these results. The second approach corresponds to the calculation of the EBS of a random configuration on a large supercell. In this work, the latter approach was employed in a supercell of 96 atoms. The EBS of the different compositions is presented in Fig. 8. The energy scale is referenced at the Fermi level.

Since the PBE functional was used in order to reduce the computational cost compared to the HSE calculations, the band gaps are severely underestimated as shown in Fig. 8. However, the results are still informative since they are qualitatively similar for both functionals. Perturbations in the band structure appear in the form of broadening of the bands. Minimal broadening is observed in the vicinity of the Γ point, while significant perturbations are observed along the A-H-K path, both for the valence and the conduction bands, as shown in Fig. 8. The characteristic band inversion of AlN around the Γ point at the top of the valence band can be observed in the $Al_{0.75}Ga_{0.25}N$ alloy. The band gap widens with increasing aluminum content and the width of the valence band decreases, in accordance with previous VCA calculations [95].

IV. DISCUSSION

The concept of the local potential depth was employed to investigate the local stability of the alloys. Locally stable ground states seem to appear for the compositions of $x = 0.333$, 0.5, and 0.667. However, the values of the local potential depths are less than 2 meV/cation indicating fairly weak stability. At growth temperatures, the thermal energy $k_B T$ exceeds 80 meV, which is indicative of the weakness of the local potential depths. Besides, the concept of the local stability applies only to the lowest-energy configurations. In the case of the random alloys, the global concavity is restored. Regions of local convexity have been reported for the system of wurtzite BeZnO [96] and are present in other systems as well [97,98].

Woicik *et al.* [20] investigated experimentally the ordering of AlGaN alloys for $x = 0.2$ and 0.45. According to their findings, the low aluminum content alloy was ordered with pure gallium layers along the [0001] direction. Additionally, they argued that even though strong ordering is maintained, mixed layers appear with increasing aluminum content. Our results agree with the appearance of pure gallium layers along the [0001] direction for the low aluminum content alloys. Specifically, pure gallium (aluminum) layers appeared in the lowest formation energy structures for $x = 0.125$ and 0.167 ($x = 0.833$ and 0.875). Pure layers of either cation were not observed for the lowest-energy configurations in the [0001] direction for compositions between $x = 0.25$ and 0.75. In general, the calculations showed that the extreme compositions favor pure cation layers, while the intermediate compositions favor better mixing, supporting the experimental findings only for the extreme compositions. Therefore, the question of the existence of ordering in the intermediate compositions still remains.

A characteristic case of ordering in a III-V semiconductor alloy system is the case of GaInP. In this system, superlattices emerge in the [111] direction [99]. For this particular system, the ordering was attributed to surface phenomena rather than bulk thermodynamics [100,101]. In the case of III-nitrides, Northrup *et al.* [102] investigated the system of InGaN and they reported that the ordering in this system is driven kinetically by surface phenomena. Our results support the notion of surface-driven phenomena for the emergence of ordering in intermediate compositions in the AlGaN system since well-mixed configurations are more energetically favorable. Previous works have also shown that surface kinetics and preferential attachment are the driven mechanisms for the ordering appearing in AlGaN [103,104]. As a further note, the high symmetry of the wurtzite crystal leads to direction-dependent mixing. In other words, while excellent mixing is achieved along a certain direction, superlattice structures emerge along a different direction. For instance, in the case of $x = 0.25$, shown in Fig. 3, monolayers and bilayers of pure gallium emerge along the a and m plane, respectively.

Limiting the discussion on the superlattices of pure gallium and aluminum layers along the [0001] direction, the formation energy was found to decrease with increasing thickness of the consecutive layers of the minority cation. This can be attributed to strain interactions, which favor the separation of the cations at different layers as a strain relief mechanism. The band gaps of these configurations were found to decrease with increasing thickness of the minority cation layers. The same dependence was reported in the work of Cui *et al.* [88], where GaN/AlN superlattices of thickness of up to 14 layers were investigated. This result is expected since decreasing the thickness of the minority cation layer increases the quantum confinement, causing the band gap to increase.

It is worth mentioning again the issue of the miscibility gap in III-nitrides, even though it is beyond the scope of this work. As discussed earlier, the presence of In induces large mismatch causing the spinodal decomposition of the InGaN alloys into In-rich and In-poor phases [8–13]. The same can be said for InAlN as well [14,15]. The situation is even worse in the case of BGaN and BAlN where the boron incorporation is typically less than 3% [15,105–107]. The electronic properties of the above-mentioned materials have been previously investigated [108–111]. AlGaN is an exception due to the relatively small lattice mismatch between GaN and AlN. The critical temperature for the miscibility gap is estimated theoretically at 70 K, indicating that solid solutions of any composition are possible for AlGaN [15].

The bowing parameter of AlGaN based on experimental evidence, ranges from -0.8 to $+2.6$ eV [24–34], even though the reports of upward (negative) bowing have not been reproduced [29,31]. Our results indicate that the bowing parameter depends strongly on the ordering of the alloy. For perfect mixing, no bowing is observed and the band gap varies linearly between the pure phases. The random alloys yield a bowing parameter of 0.36 eV both in PBE and HSE calculations. However, as shown in Fig. 4, the random alloys exhibit quite large band gaps compared to other configurations. Thus, the bowing parameter could reasonably take even larger values depending on the kind of ordering considered. Finally, stronger bowing is observed for increasing aluminum content.

Moreover, the calculated band offset between the pure phases was 0.40 and 0.46 eV, obtained by the a- and m-plane surfaces, respectively. Since both surfaces were nonpolar, any effects that arise from the polarization of the crystal were eliminated and both surfaces should in principle yield the same result. The small difference of 0.06 eV in the band offset of the pure phases does not affect the results and is indicative of the computational uncertainties. This difference has also been reported in previous GW calculations [64]. The band offset dependence on the composition was investigated with the $Al_{0.5}Ga_{0.5}N$ alloy. A strong dependence on the ordering was observed for the valence band offset, i.e., both upward and downward deviations from linearity were observed. Well-mixed configurations yield downward deviation from linearity, while upward deviation is observed for poorly mixed configurations.

The band structures of the wurtzite phases of GaN and AlN are qualitatively similar in general. Some minor differences are observed along the A-H-K path [112]. Therefore, minor perturbations are observed in the EBS of the random alloys around the Γ point, while some broadening is observed in the band structure along the A-H-K path. On the contrary, the band structures of the cubic phases of GaN and AlN are quite different, with cubic AlN being an indirect semiconductor. Landmann *et al.* [71] determined that the crossover composition for which the alloy transitions from direct to indirect gap occurs at around 63% Al content. In the case of cubic AlGaN, the EBS is expected to exhibit large perturbations.

At this point, it is worth commenting on the approach of using different mixing parameters for the HSE calculations of the alloys at different compositions since the structural properties of a material, its energy eigenvalues, as well as its total energy are affected by changing the mixing parameter. The effect on the structural properties is directly related to the lattice constant, the energy eigenvalues are essential for determining the band gap, while the total energy is crucial for obtaining properties such as the formation energy of the alloys. As shown in Eq. (1), the formation energy of a given configuration at a certain composition depends on the total energies of the pure phases and the total energy of the corresponding configuration. Therefore, the formation energies rely on the comparison of the total energies of three different systems. Since the total energies are affected by the mixing parameter, varying the mixing parameter of each composition in this case would significantly impact the results. In such cases, PBE calculations like the ones presented in Fig. 2 are more appropriate.

However, not all properties suffer from a variable mixing parameter in the HSE calculations. For instance, unlike the formation energies, the lattice constant is an inherent property of the material, which is obtained independently for each system. Therefore, the lattice constants can be investigated using different mixing parameters. Figure 1 shows the excellent agreement between PBE (no mixing parameter) and HSE (variable mixing parameter) for the slope of the line connecting the lattice constants of the different compositions. The PBE results overestimate the lattice constant, as expected, while the HSE results are in excellent agreement with experimental data, as presented in Table I. Furthermore, the band gap of each material is obtained as the energy difference of the eigenvalues of the lowest unoccupied state and the highest occupied state. The eigenvalues are also obtained independently for each system and not as a relative quantity in comparison to other materials. Therefore, an optimal mixing parameter can be used to describe each system independently, as long as the same mixing parameter is used for a given composition.

Our approach for determining the band alignments relies on the determination of the IP/EA of each material. This approach offers a significant advantage on the matter of the variable mixing parameter since the IP/EA of each material is an inherent property of the material and is obtained independently. Nevertheless, it is informative to investigate the effect of a common mixing parameter on the band offsets. The mixing parameter affects neither the position of the vacuum level nor the average electrostatic potential at the center of the slab. Instead, the mixing parameter affects only the bulk eigenvalues. A common mixing parameter leads to either the overestimation or the underestimation of the band gap of one

of the two systems under investigation. Due to the wrong description of the band gap in the case of a common mixing parameter, the valence band offset is affected by 0.1 eV with respect to the results obtained for variable mixing parameters. The fact that both the vacuum level and the average electrostatic potential are unaffected by the mixing parameter is indicative of the need to properly account for the band gap of each material, in order to obtain the correct band alignment. Evidence of this is provided in the Supplemental Material [113].

Finally, even though the heterostructure method [72,73] was not adopted in this work for the determination of the band offsets, it is worth mentioning the effects of the mixing parameter in this method as well, both for completeness and to demonstrate the similarities to our approach. In the heterostructure approach, the two different materials coexist at the same supercell. Therefore, the use of a single mixing parameter describing both materials is unavoidable in this approach. Additionally, the eigenvalues of the valence band maximum and conduction band minimum are obtained by separate bulk calculations, similar to the IP/EA approach. Alkauskas *et al.* [73] demonstrated the merits of using the optimal mixing parameter of each system, in order to properly account for the correct band gap of each material involved in the calculation. The scheme proposed by Alkauskas *et al.* [73] involves bulk calculations using the optimal mixing parameter of each material while the average mixing parameter is used for the heterostructure calculations where a single mixing parameter is unavoidable. According to Alkauskas *et al.* [73], this mixed scheme provides a striking improvement in the theoretical estimation of band offsets. In the IP/EA band alignment approach that was adopted in this work, the reference levels, which are the vacuum level and the average electrostatic potential, are unaffected by the mixing parameter [113], indicating that obtaining the correct IP/EA is a matter of describing the band gap properly. Similarly, Alkauskas *et al.* [73] showed that the reference levels in the heterostructure approach, which are the average electrostatic potentials at each side of the interface, are also unaffected by different mixing parameters, thus, indicating the need to just properly account for the band gap in the heterostructure approach as well.

V. CONCLUSION

The dependence of the structural and electronic properties of AlGaN alloys on the composition and the atomic ordering was investigated employing first-principles calculations. Both standard and hybrid density functionals were used. The investigated properties include the stability of the alloys, their band gaps and band offsets, as well as their effective band structures.

The stability of the alloy in different compositions was derived by formation energy calculations on all the distinct atomic configurations that can be modeled in supercells of up to 16 atoms. Overall, the general concavity of the results indicated the lack of ground states for the intermediate compositions. However, states exhibiting local convexity were observed for $x = 0.333$, 0.5, and 0.667. Well-mixed configurations were found to yield the lowest formation energies, while structures exhibiting poor mixing or long-range ordering were less thermodynamically favorable. Particularly, the formation energy of the superlattices along the [0001] direction was influenced by the thickness of the consecutive layers of the minority cation, with increasing thickness yielding lower formation energy. Yet, relying on the bulk thermodynamics, the formation of the [0001] superlattices could not be explained, especially for the intermediate compositions. Instead, we attribute the preference to the [0001] superlattices on surface phenomena during growth.

The electronic properties of the alloys were significantly affected by the different types of atomic orderings observed in the alloys. Well-mixed configurations typically produced large band gaps, following minimal downward bowing dependence on the composition of the alloy. Specifically, for the lowest formation energy configurations, the dependence was linear. On the other hand, poorly mixed configurations exhibited larger deviations from linearity, causing an increase in the bowing parameter. Overall, depending on the atomic ordering, the bowing parameter ranges from zero to large positive values. Additionally, the atomic ordering affected the band offsets of the alloys with respect to the pure phases. A downward deviation from the linear band offset connecting the pure phases was observed for well-mixed alloys, while upward deviation was exhibited by poorly mixed configurations. The ionization potentials and the electron affinities were calculated for the pure phases and good agreement with previously reported experimental and theoretical data is observed. Regarding the $Al_{0.5}Ga_{0.5}N$ alloy, the different kinds of ordering were found to affect mainly the ionization potential of the material, hence, the top of the valence band with respect to the vacuum level. The effective band structures of the random alloys of compositions $x = 0.25$, 0.5, and 0.75 were investigated and minimal perturbations were observed around the Γ point. Additionally, the shrinking of the width of the valence band was observed with increasing aluminum content.

ACKNOWLEDGMENTS

The authors gratefully acknowledge fruitful discussions with T. D. Moustakas. This work was supported by the U. S. Army Research Laboratory through the Collaborative Research Alliance for Multi-Scale multidisciplinary Modeling of Electronic Materials (Grant No. W911NF-12-2-0023). The computational resources were provided by the DoD HPC Systems and the 2014 Army Research Office DURIP Award (Grant No. W911NF-14-1-0432). Atomistic visualizations were generated using the software VESTA [114].

[1] S. Pimputkar, J. S. Speck, S. P. DenBaars, and S. Nakamura, Nat. Photonics **3**, 180 (2009).

[2] A. Khan, K. Balakrishnan, and T. Katona, Nat. Photonics **2**, 77 (2008), review article.

[3] U. K. Mishra, P. Parikh, and Y. F. Wu, Proc. IEEE **90**, 1022 (2002).

[4] R. Dahal, J. Li, K. Aryal, J. Y. Lin, and H. X. Jiang, Appl. Phys. Lett. **97**, 073115 (2010).

[5] M. Levinshtein, S. Rumyantsev, and M. Shur, *Properties of Advanced Semiconductor Materials: GaN, AlN, InN, BN, SiC, SiGe* (Wiley, New York, 2001).

[6] I. Ho and G. B. Stringfellow, Appl. Phys. Lett. **69**, 2701 (1996).

[7] T. Matsuoka, Appl. Phys. Lett. **71**, 105 (1997).

[8] L. K. Teles, J. Furthmüller, L. M. R. Scolfaro, J. R. Leite, and F. Bechstedt, Phys. Rev. B **62**, 2475 (2000).

[9] R. Singh, D. Doppalapudi, T. D. Moustakas, and L. T. Romano, Appl. Phys. Lett. **70**, 1089 (1997).

[10] M. D. McCluskey, L. T. Romano, B. S. Krusor, D. P. Bour, N. M. Johnson, and S. Brennan, Appl. Phys. Lett. **72**, 1730 (1998).

[11] S. Y. Karpov, MRS Internet J. Nitride Semicond. Res. **3**, e16 (1998).

[12] C. K. Gan, Y. P. Feng, and D. J. Srolovitz, Phys. Rev. B **73**, 235214 (2006).

[13] A. I. Duff, L. Lymperakis, and J. Neugebauer, Phys. Status Solidi B **252**, 855 (2015).

[14] J. Palisaitis, C.-L. Hsiao, L. Hultman, J. Birch, and P. O. Å. Persson, Sci. Rep. **7**, 44390 (2017).

[15] M. Razeghi and M. Henini, *Optoelectronic Devices: III-nitrides*, Vol. 3 (Elsevier, Amsterdam, 2004), Chap. 16.

[16] E. A. Albanesi, W. R. L. Lambrecht, and B. Segall, Phys. Rev. B **48**, 17841 (1993).

[17] D. Korakakis, K. F. Ludwig, and T. D. Moustakas, Appl. Phys. Lett. **71**, 72 (1997).

[18] B. Neubauer, A. Rosenauer, D. Gerthsen, O. Ambacher, and M. Stutzmann, Appl. Phys. Lett. **73**, 930 (1998).

[19] E. Iliopoulos, K. F. Ludwig, T. D. Moustakas, and S. N. G. Chu, Appl. Phys. Lett. **78**, 463 (2001).

[20] J. C. Woicik, K. F. Ludwig, and T. D. Moustakas, Appl. Phys. Lett. **100**, 162105 (2012).

[21] A. G. Norman, R. France, and A. J. Ptak, J. Vac. Sci. Technol., B: Microelectron. Process. Phenom. **29**, 03C121 (2011).

[22] M. A. Shahid, S. Mahajan, D. E. Laughlin, and H. M. Cox, Phys. Rev. Lett. **58**, 2567 (1987).

[23] M. Marques, L. K. Teles, and L. G. Ferreira, Phys. Rev. B **75**, 033201 (2007).

[24] F. Yun, M. A. Reshchikov, L. He, T. King, H. Morkoç, S. W. Novak, and L. Wei, J. Appl. Phys. **92**, 4837 (2002).

[25] M. A. Khan, R. A. Skogman, R. G. Schulze, and M. Gershenzon, Appl. Phys. Lett. **43**, 492 (1983).

[26] S. Yoshida, S. Misawa, and S. Gonda, J. Appl. Phys. **53**, 6844 (1982).

[27] H. Angerer, D. Brunner, F. Freudenberg, O. Ambacher, M. Stutzmann, R. Höpler, T. Metzger, E. Born, G. Dollinger, A. Bergmaier, S. Karsch, and H.-J. Körner, Appl. Phys. Lett. **71**, 1504 (1997).

[28] Y. Koide, H. Itoh, M. R. H. Khan, K. Hiramatu, N. Sawaki, and I. Akasaki, J. Appl. Phys. **61**, 4540 (1987).

[29] S. R. Lee, A. F. Wright, M. H. Crawford, G. A. Petersen, J. Han, and R. M. Biefeld, Appl. Phys. Lett. **74**, 3344 (1999).

[30] W. Shan, J. W. Ager, K. M. Yu, W. Walukiewicz, E. E. Haller, M. C. Martin, W. R. McKinney, and W. Yang, J. Appl. Phys. **85**, 8505 (1999).

[31] I. Vurgaftman and J. R. Meyer, J. Appl. Phys. **94**, 3675 (2003).

[32] R. R. Pelá, C. Caetano, M. Marques, L. G. Ferreira, J. Furthmüller, and L. K. Teles, Appl. Phys. Lett. **98**, 151907 (2011).

[33] J. Wu, W. Walukiewicz, K. Yu, J. Ager, S. Li, E. Haller, H. Lu, and W. J. Schaff, Solid State Commun. **127**, 411 (2003).

[34] Z. Dridi, B. Bouhafs, and P. Ruterana, Semicond. Sci. Technol. **18**, 850 (2003).

[35] Z. Sitar, M. Paisley, B. Yan, R. Davis, J. Ruan, and J. Choyke, Thin Solid Films **200**, 311 (1991).

[36] A. Rizzi, R. Lantier, F. Monti, H. Lüth, F. D. Sala, A. Di Carlo, and P. Lugli, J. Vac. Sci. Technol., B: Microelectron. Process. Phenom. **17**, 1674 (1999).

[37] J. R. Waldrop and R. W. Grant, Appl. Phys. Lett. **68**, 2879 (1996).

[38] J. Baur, K. Maier, M. Kunzer, U. Kaufmann, and J. Schneider, Appl. Phys. Lett. **65**, 2211 (1994).

[39] P. G. Moses, M. Miao, Q. Yan, and C. G. Van de Walle, J. Chem. Phys. **134**, 084703 (2011).

[40] E. A. Albanesi, W. R. L. Lambrecht, and B. Segall, J. Vac. Sci. Technol., B: Microelectron. Process. Phenom. **12**, 2470 (1994).

[41] S. Satpathy, Z. S. Popovic, and W. C. Mitchel, J. Appl. Phys. **95**, 5597 (2004).

[42] M. Buongiorno Nardelli, K. Rapcewicz, and J. Bernholc, Phys. Rev. B **55**, R7323(R) (1997).

[43] N. Binggeli, P. Ferrara, and A. Baldereschi, Phys. Rev. B **63**, 245306 (2001).

[44] F. Bernardini and V. Fiorentini, Phys. Rev. B **57**, R9427 (1998).

[45] J. A. Majewski, G. Zandler, and P. Vogl, Semicond. Sci. Technol. **13**, A90 (1998).

[46] D. Cociorva, W. G. Aulbur, and J. W. Wilkins, Solid State Commun. **124**, 63 (2002).

[47] A. Rubio, J. L. Corkill, and M. L. Cohen, Phys. Rev. B **49**, 1952 (1994).

[48] S. Wei and A. Zunger, Appl. Phys. Lett. **69**, 2719 (1996).

[49] C. G. Van de Walle and J. Neugebauer, Nature (London) **423**, 626 (2003).

[50] P. Hohenberg and W. Kohn, Phys. Rev. **136**, B864 (1964).

[51] W. Kohn and L. J. Sham, Phys. Rev. **140**, A1133 (1965).

[52] P. E. Blöchl, Phys. Rev. B **50**, 17953 (1994).

[53] G. Kresse and D. Joubert, Phys. Rev. B **59**, 1758 (1999).

[54] G. Kresse and J. Furthmüller, Phys. Rev. B **54**, 11169 (1996).

[55] J. P. Perdew, K. Burke, and M. Ernzerhof, Phys. Rev. Lett. **77**, 3865 (1996).

[56] J. P. Perdew, K. Burke, and M. Ernzerhof, Phys. Rev. Lett. **78**, 1396 (1997).

[57] J. P. Perdew, A. Ruzsinszky, G. I. Csonka, O. A. Vydrov, G. E. Scuseria, L. A. Constantin, X. Zhou, and K. Burke, Phys. Rev. Lett. **100**, 136406 (2008).

[58] J. Heyd, G. E. Scuseria, and M. Ernzerhof, J. Chem. Phys. **118**, 8207 (2003).

[59] J. Heyd, G. E. Scuseria, and M. Ernzerhof, J. Chem. Phys. **124**, 219906 (2006).

[60] A. van de Walle, M. D. Asta, and G. Ceder, CALPHAD: Comput. Coupling Phase Diagrams Thermochem. **26**, 539 (2002).

[61] A. van de Walle, CALPHAD: Comput. Coupling Phase Diagrams Thermochem. **33**, 266 (2009).

[62] L. Ferreira, S.-H. Wei, and A. Zunger, Int. J. Supercomput. Applicat. **5**, 34 (1991).

[63] S. V. Barabash, V. Blum, S. Müller, and A. Zunger, Phys. Rev. B **74**, 035108 (2006).

[64] Y. Hinuma, A. Grüneis, G. Kresse, and F. Oba, Phys. Rev. B **90**, 155405 (2014).

[65] B. Höffling, A. Schleife, C. Rödl, and F. Bechstedt, Phys. Rev. B **85**, 035305 (2012).

[66] R. Anderson, Solid-State Electron. **5**, 341 (1962).

[67] C. Mitra, B. Lange, C. Freysoldt, and J. Neugebauer, Phys. Rev. B **84**, 193304 (2011).

[68] E. A. Kraut, R. W. Grant, J. R. Waldrop, and S. P. Kowalczyk, Phys. Rev. B **28**, 1965 (1983).

[69] J. Tersoff, Phys. Rev. Lett. **52**, 465 (1984).

[70] A. Schleife, F. Fuchs, C. Rödl, J. Furthmüller, and F. Bechstedt, Appl. Phys. Lett. **94**, 012104 (2009).

[71] M. Landmann, E. Rauls, and W. G. Schmidt, Phys. Rev. B **95**, 155310 (2017).

[72] Y. Hinuma, F. Oba, Y. Kumagai, and I. Tanaka, Phys. Rev. B **88**, 035305 (2013).

[73] A. Alkauskas, P. Broqvist, F. Devynck, and A. Pasquarello, Phys. Rev. Lett. **101**, 106802 (2008).

[74] C. G. Van de Walle, Phys. Rev. B **39**, 1871 (1989).

[75] A. Baldereschi, S. Baroni, and R. Resta, Phys. Rev. Lett. **61**, 734 (1988).

[76] J. S. Faulkner and G. M. Stocks, Phys. Rev. B **21**, 3222 (1980).

[77] N. Lothar, Ann. Phys. **401**, 607 (1931).

[78] V. Popescu and A. Zunger, Phys. Rev. Lett. **104**, 236403 (2010).

[79] V. Popescu and A. Zunger, Phys. Rev. B **85**, 085201 (2012).

[80] P. V. C. Medeiros, S. Stafström, and J. Björk, Phys. Rev. B **89**, 041407 (2014).

[81] P. V. C. Medeiros, S. S. Tsirkin, S. Stafström, and J. Björk, Phys. Rev. B **91**, 041116 (2015).

[82] H. Schulz and K. Thiemann, Solid State Commun. **23**, 815 (1977).

[83] A. Kyrtsos, M. Matsubara, and E. Bellotti, Phys. Rev. B **93**, 245201 (2016).

[84] Q. Yan, P. Rinke, M. Scheffler, and C. G. Van de Walle, Appl. Phys. Lett. **95**, 121111 (2009).

[85] A. R. Denton and N. W. Ashcroft, Phys. Rev. A **43**, 3161 (1991).

[86] S. Lee, C. Freysoldt, and J. Neugebauer, Phys. Rev. B **90**, 245301 (2014).

[87] L. Lymperakis, T. Schulz, C. Freysoldt, M. Anikeeva, Z. Chen, X. Zheng, B. Shen, C. Chèze, M. Siekacz, X. Q. Wang, M. Albrecht, and J. Neugebauer, Phys. Rev. Mater. **2**, 011601 (2018).

[88] X. Y. Cui, B. Delley, and C. Stampfl, J. Appl. Phys. **108**, 103701 (2010).

[89] I. Csik, S. P. Russo, and P. Mulvaney, Chem. Phys. Lett. **414**, 322 (2005).

[90] S. P. Grabowski, M. Schneider, H. Nienhaus, W. Mönch, R. Dimitrov, O. Ambacher, and M. Stutzmann, Appl. Phys. Lett. **78**, 2503 (2001).

[91] K. M. Tracy, W. J. Mecouch, R. F. Davis, and R. J. Nemanich, J. Appl. Phys. **94**, 3163 (2003).

[92] M. Benjamin, M. Bremser, T. Weeks, S. King, R. Davis, and R. Nemanich, Appl. Surf. Sci. **104-105**, 455 (1996).

[93] C. I. Wu and A. Kahn, J. Vac. Sci. Technol., B: Microelectron. Process. Phenom. **16**, 2218 (1998).

[94] C. I. Wu, A. Kahn, E. S. Hellman, and D. N. E. Buchanan, Appl. Phys. Lett. **73**, 1346 (1998).

[95] E. Bellotti and F. Bertazzi, J. Appl. Phys. **111**, 103711 (2012).

[96] X. F. Fan, Z. Zhu, Y.-S. Ong, Y. M. Lu, Z. X. Shen, and J.-L. Kuo, Appl. Phys. Lett. **91**, 121121 (2007).

[97] Z. T. Y. Liu, B. P. Burton, S. V. Khare, and D. Gall, J. Phys.: Condens. Matter **29**, 035401 (2017).

[98] R. Chinnappan, CALPHAD: Comput. Coupling Phase Diagrams Thermochem. **39**, 33 (2012).

[99] T. D. Moustakas, MRS Commun. **6**, 247 (2016).

[100] R. Osório, J. E. Bernard, S. Froyen, and A. Zunger, Phys. Rev. B **45**, 11173 (1992).

[101] L. C. Su, I. H. Ho, and G. B. Stringfellow, Appl. Phys. Lett. **65**, 749 (1994).

[102] J. E. Northrup, L. T. Romano, and J. Neugebauer, Appl. Phys. Lett. **74**, 2319 (1999).

[103] M. Benamara, L. Kirste, M. Albrecht, K. W. Benz, and H. P. Strunk, Appl. Phys. Lett. **82**, 547 (2003).

[104] M. Albrecht, L. Lymperakis, J. Neugebauer, J. E. Northrup, L. Kirste, M. Leroux, I. Grzegory, S. Porowski, and H. P. Strunk, Phys. Rev. B **71**, 035314 (2005).

[105] L. K. Teles, L. M. R. Scolfaro, J. R. Leite, J. Furthmüller, and F. Bechstedt, Appl. Phys. Lett. **80**, 1177 (2002).

[106] C. H. Wei, Z. Y. Xie, J. H. Edgar, K. C. Zeng, J. Y. Lin, H. X. Jiang, J. Chaudhuri, C. Ignatiev, and D. N. Braski, J. Electron. Mater. **29**, 452 (2000).

[107] M. Shibata, M. Kurimoto, J. Yamamoto, T. Honda, and H. Kawanishi, J. Cryst. Growth **189-190**, 445 (1998).

[108] P. G. Moses and C. G. Van de Walle, Appl. Phys. Lett. **96**, 021908 (2010).

[109] S. Schulz, M. A. Caro, L.-T. Tan, P. J. Parbrook, R. W. Martin, and E. P. O'Reilly, Appl. Phys. Express **6**, 121001 (2013).

[110] J.-X. Shen, D. Wickramaratne, and C. G. Van de Walle, Phys. Rev. Mater. **1**, 065001 (2017).

[111] T. Akiyama, K. Nakamura, and T. Ito, Appl. Phys. Express **11**, 025501 (2018).

[112] Q. Yan, P. Rinke, A. Janotti, M. Scheffler, and C. G. Van de Walle, Phys. Rev. B **90**, 125118 (2014).

[113] See Supplemental Material at http://link.aps.org/supplemental/10.1103/PhysRevB.99.035201 for further details on the effects of the mixing parameter in the determination of the IP/EA. The Supplemental Material contains Ref. [39].

[114] K. Momma and F. Izumi, J. Appl. Crystallogr. **44**, 1272 (2011).